




 Cite this: *RSC Adv.*, 2021, 11, 11702

# Enhanced charge separation in TiO<sub>2</sub>/nanocarbon hybrid photocatalysts through coupling with short carbon nanotubes†

 Ahmed Al Mayyahi,<sup>a</sup> Brian M. Everhart,<sup>a</sup> Tej B. Shrestha,<sup>b</sup> Tyson C. Back <sup>c</sup> and Placidus B. Amama <sup>\*a</sup>

The interfacial contact between TiO<sub>2</sub> and graphitic carbon in a hybrid composite plays a critical role in electron transfer behavior, and in turn, its photocatalytic efficiency. Herein, we report a new approach for improving the interfacial contact and delaying charge carrier recombination in the hybrid by wrapping short single-wall carbon nanotubes (SWCNTs) on TiO<sub>2</sub> particles (100 nm) via a hydration-condensation technique. Short SWCNTs with an average length of 125 ± 90 nm were obtained from an ultrasonication-assisted cutting process of pristine SWCNTs (1–3 μm in length). In comparison to conventional TiO<sub>2</sub>–SWCNT composites synthesized from long SWCNTs (1.2 ± 0.7 μm), TiO<sub>2</sub> wrapped with short SWCNTs showed longer lifetimes of photogenerated electrons and holes, as well as a superior photocatalytic activity in the gas-phase degradation of acetaldehyde. In addition, upon comparison with a TiO<sub>2</sub>–nanographene “quasi-core-shell” structure, TiO<sub>2</sub>–short SWCNT structures offer better electron-capturing efficiency and slightly higher photocatalytic performance, revealing the impact of the dimensions of graphitic structures on the interfacial transfer of electrons and light penetration to TiO<sub>2</sub>. The engineering of the TiO<sub>2</sub>–SWCNT structure is expected to benefit photocatalytic degradation of other volatile organic compounds, and provide alternative pathways to further improve the efficiency of other carbon-based photocatalysts.

 Received 4th January 2021  
 Accepted 10th March 2021

DOI: 10.1039/d1ra00045d

[rsc.li/rsc-advances](http://rsc.li/rsc-advances)

## 1. Introduction

Rapid recombination of photogenerated electron–hole pairs is one of the major limitations of utilizing TiO<sub>2</sub> photocatalysts in applications such as water treatment,<sup>1–3</sup> air purification<sup>4–9</sup> bacterial and viral inactivation,<sup>10,11</sup> and self-cleaning glasses.<sup>12–14</sup> Most of the photogenerated electron–hole pairs recombine within 10 picoseconds (ps), which is very short compared to the 100 ps typically required for redox reactions. As a result, only a small portion (~10 percent) of the photogenerated charges, as revealed by time-resolved absorption spectroscopic studies, remain alive and able to participate in pollutant decomposition, resulting in limited photocatalytic activity.<sup>15,16</sup> A number of studies have shown that inhibition of charge recombination and remarkable enhancement in photocatalytic efficiency of TiO<sub>2</sub> can be achieved by coupling with carbon nanomaterials such as carbon nanotubes (CNTs), graphene, and fullerene.<sup>17–21</sup>

The coupling leads to formation of a Schottky barrier, through which electrons efficiently travel from TiO<sub>2</sub> with a higher Fermi level to the carbon nanomaterial with a lower Fermi level until equilibrium is attained.<sup>22,23</sup> In addition, the high electron-storage capacity of the graphitic structure (one electron per 32 carbon atoms) can serve as electron reservoirs or sinks, decreasing the recombination probability of the photogenerated charges in the hybrid material and enhancing photocatalytic activity.<sup>22</sup>

The improved charge separation in TiO<sub>2</sub>–nanocarbon hybrid structures depends largely on the quality of interfacial contact between TiO<sub>2</sub> and the graphitic structure, and the structural and surface properties of the hybrid components.<sup>21,24–30</sup> A knowledge gap that still exists is how the graphitic structures and their geometries affect the coupling and interfacial contacts of the components in the hybrid. The rate of electron transport and subsequent separation of photogenerated charges in conventional TiO<sub>2</sub>–nanocarbon composites are still hampered by nonuniform coating or poor dispersion induced by TiO<sub>2</sub> aggregation on graphene sheets or CNT walls. Therefore, in light of the great promise shown by TiO<sub>2</sub>–nanocarbon hybrids in photocatalysis, research efforts have focused on tailoring the heterojunctions and schottky barriers to achieve efficient shuttling of electrons and promote electron–hole separation, as well as induce visible light excitation. It is well-established in the literature that charge recombination is inhibited on

<sup>a</sup>Tim Taylor Department of Chemical Engineering, Kansas State University, Manhattan, KS 66506, USA. E-mail: [pamama@ksu.edu](mailto:pamama@ksu.edu)

<sup>b</sup>Nanotechnology Innovation Center of Kansas State, Manhattan, KS 66506, USA

<sup>c</sup>Materials and Manufacturing Directorate, Air Force Research Laboratory, Wright-Patterson AFB, OH 45433, USA

† Electronic supplementary information (ESI) available. See DOI: 10.1039/d1ra00045d



a variety of TiO<sub>2</sub>-CNT hybrids consisting of a thin, uniform TiO<sub>2</sub> layer on individual multi-walled CNTs (MWCNTs) or TiO<sub>2</sub> aggregates supported on CNTs.<sup>29,31-34</sup> However, the trade-off relation between electron-hole concentration and separation efficiency in conventional TiO<sub>2</sub>-coated CNT composites remains a significant impediment to maximizing the photocatalytic activity.<sup>28</sup> To this end, TiO<sub>2</sub> wrapped with graphene has been considered as an alternative to the TiO<sub>2</sub>/CNT core-shell (or TiO<sub>2</sub>-coated CNT) structure, as the concentration of photo-generated charges can be optimized without sacrificing separation efficiency.<sup>19,35</sup>

Significant differences exist in hybrid structures formed with either CNTs or graphene. Graphene, a two-dimensional (2D) structure with several nanometers of width and high stacking tendency, can generate a “shell-like” structure consisting of several graphene layers on TiO<sub>2</sub>, preventing light penetration.<sup>36,37</sup> Another complication associated with graphene is the unavoidable electron scattering that may reduce the electron transport rate and promote charge recombination.<sup>37</sup> On the other hand, harnessing the one-dimensional (1D) single-wall CNT (SWCNT) structures in TiO<sub>2</sub> hybrids not only provides well-defined routes for electron transport, but also their small size compared to MWCNTs and graphene sheets provide a degree of freedom for optimizing charge separation without compromising light absorption.<sup>38-42</sup> A consensus from the aforementioned studies is that the structure of nanocarbons (*i.e.*, the size of graphene or length of CNTs) is a crucial factor in controlling the quality of interfacial contact and subsequent charge separation. In particular, Kim *et al.*<sup>36</sup> revealed a superior photocatalytic activity for TiO<sub>2</sub> hybrids formed with nano-sized graphene (or nanographene) sheets in comparison to those formed with micro-sized graphene; the wrapping of nanographene on TiO<sub>2</sub> particles in the former hybrid maximized the interfacial contact between the components, resulting in superior charge separation and photocatalytic activity. Similarly, we hypothesize that cutting long SWCNTs into high populations of open-ended tubes with high degrees of functionalization and density of active sites, as well as short lengths that can effectively wrap a large TiO<sub>2</sub> particle (~100 nm), can lead to enhanced interactions with TiO<sub>2</sub> particles that will promote the photocatalytic process. Although many studies have investigated the influence of coupling SWCNTs with TiO<sub>2</sub>, all reported works employed SWCNTs with lengths in the micrometer range.

In this study, we report for the first time the wrapping of large TiO<sub>2</sub> particles (~100 nm) with short SWCNTs (125 ± 90 nm in length) obtained from an ultrasonication-assisted cutting process. The resulting TiO<sub>2</sub>-SWCNT hybrid photocatalyst exhibits enhanced interfacial contact and charge separation. The short, highly functionalized and dispersed SWCNTs, in the presence of TiO<sub>2</sub>, initiated formation of Ti-O-C bonds *via* intermolecular interactions, resulting in TiO<sub>2</sub> nanoparticles or nanoparticle aggregates that are partially wrapped by SWCNTs. In comparison to conventional TiO<sub>2</sub>-SWCNT composites synthesized using long SWCNTs (1.2 ± 0.7 μm), TiO<sub>2</sub> wrapped with short SWCNTs showed longer lifetimes of photogenerated electrons and holes, as well as a superior photocatalytic activity in the gas-phase degradation of acetaldehyde. In addition, upon comparison with

a TiO<sub>2</sub>-nanographene “quasi-core-shell” structure, the novel TiO<sub>2</sub>-SWCNT composite offers superior electron-capturing efficiency and slightly higher photocatalytic performance, revealing the impact of the dimension of graphitic structures on the interfacial transfer of electrons and light penetration to TiO<sub>2</sub>.

## 2. Experimental section

### 2.1. Synthesis of TiO<sub>2</sub>-SWCNT composites

Purified SWCNTs (1–2 nm in diameter and 1–3 μm in length) were functionalized by refluxing with HNO<sub>3</sub> (70%) at 150 °C for two hours. A known amount of functionalized SWCNTs were dispersed in ethanol and sonicated at 25 °C for four hours to produce the short SWCNTs. After the sonication-assisted cutting process, the resulting suspension was allowed to settle for 15 minutes and the supernatant was slowly added to the TiO<sub>2</sub>-ethanol dispersion (50 mg in 50 mL ethanol) under sonication, followed by robust stirring overnight at pH = 3.4. The sonicator (Branson, CPX5800H) operated at 100 W and 40 kHz. The TiO<sub>2</sub> particles (anatase, 99.9%, 100 nm) were purchased from US Research Nanomaterials, Inc. The TiO<sub>2</sub>-SWCNT hybrid synthesized from short SWCNTs (hereafter referred to as TiO<sub>2</sub>-short SWCNT) was collected by filtration using a membrane with average pore size of 0.2 μm and dried at 60 °C. For TiO<sub>2</sub>-SWCNT hybrids synthesized from long SWCNTs, the same procedure was followed without subjecting the long SWCNTs to ultrasonication-assisted cutting; the resulting hybrid is hereafter referred to as TiO<sub>2</sub>-long SWCNT. Unless stated otherwise, the amount of SWCNTs used in the standard sample is 1 wt%.

### 2.2. Synthesis of TiO<sub>2</sub>-nanographene composites

The graphite powder was oxidized by the modified Hummer method.<sup>43-45</sup> The graphene oxide (GO) produced was treated with a mixture of HCl and KMnO<sub>4</sub> to produce the nanographene oxide. GO (0.05 g) was dispersed in 50 mL of concentrated HCl, and then 0.05 g of KMnO<sub>4</sub> was slowly added under robust stirring. After one hour of stirring at 40 °C, the resulting slurry was cooled in an ice bath. Then, H<sub>2</sub>O<sub>2</sub> solution (5 mL H<sub>2</sub>O<sub>2</sub> and 95 mL distilled water) was slowly added with continued stirring for one hour, followed by sonication for 30 minutes to exfoliate the nanographene oxide. The final product was collected by filtration using similar conditions in Section 2.1 and oven-dried at 60 °C.

The TiO<sub>2</sub>-nanographene composite (0.7 wt% nanographene) was synthesized by dispersing a known amount of nanographene oxide in ethanol by sonication, and the resulting slurry was slowly added to the TiO<sub>2</sub>-ethanol dispersion (50 mg in 50 mL distilled water) under stirring at pH = 3.5, followed by robust stirring overnight. The brownish powder obtained was transferred to a Teflon-lined, hydrothermal synthesis autoclave reactor and heated at 120 °C for 24 hours to reduce the nanographene oxide. The final product (hereafter referred to as TiO<sub>2</sub>-nanographene) was washed repeatedly with 1 M HCl and distilled water, collected by filtration and dried at 60 °C.



### 2.3. Characterization methods

X-ray diffraction (XRD) patterns were collected on a Rigaku Miniex II X-ray diffractometer with Cu K $\alpha$  radiation ( $\lambda = 1.5418$  Å) at 40 kV and 40 mA. The Raman spectra were acquired *via* an iHR550 spectrometer with a laser excitation wavelength of 532 nm. Catalyst morphology was characterized by a field-emission scanning electron microscope (SEM, Hitachi S5200) equipped with energy-dispersive X-ray spectroscopy (EDS), and a transmission electron microscope (TEM, FEI Talos) operating at 200 kV. For TEM analysis, a small amount of the sample was dispersed in ethanol by sonication and dropped onto a copper microgrid coated with lacy carbon film. X-ray photoelectron spectroscopic (XPS) measurements were collected *via* a Kratos Ultra XPS system at  $1.0 \times 10^{-9}$  Torr. A monochromatic Al K $\alpha$  source ( $h\nu = 1486.6$  eV) operating at 10 mA and 12 keV (120 W) was used to collect the spectra. The effect of charging was reduced by a charge neutralizer. Survey spectra were collected at 160 eV pass energy with 1 eV step and 100 ms contact time. For the high-resolution scans, spectra were collected at 20 eV pass energy with 0.1 eV step and 100 ms contact time. The photoluminescence (PL) spectra were acquired *via* a spectraMax i3x multi-mode microplate reader over the range of 400–700 nm using an excitation wavelength of 360 nm.

### 2.4. Evaluation of photocatalytic activity

The photocatalytic activity was tested by measuring the change in concentration of gas phase acetaldehyde as a function of

irradiation time. The photocatalyst (100 mg) was placed in a 750 mL borosilicate batch reactor surrounded by light sources (two 25 W Sylvania 21703 (356 nm) bulbs and two 13 W Repti-Sun 10.0 UV/B bulbs (280–320 nm) with intensity of  $6.5 \text{ W m}^{-2}$ ). One thousand ppmv of acetaldehyde gas was injected into the reactor *via* a syringe. After equilibrium between gaseous and adsorbed phases was attained, UV irradiation was started and the decrease in concentration was measured *via* an SRI 310C gas chromatograph equipped with a Restek silica gel column (8046-895, 6 ft length, 2 mm ID), on-column injection, and flame ionization detector (FID). According to the experimental data, acetaldehyde degradation by TiO<sub>2</sub>-short SWCNT, TiO<sub>2</sub>-long SWCNT and TiO<sub>2</sub>-nanographene fitted to a pseudo first-order reaction represented by eqn (1):

$$\frac{c}{c_0} = e^{-kt} \quad (1)$$

where  $k$  is the apparent constant of reaction rate,  $c$  is the concentration of acetaldehyde and  $t$  is the reaction time.

## 3. Results

### 3.1. Morphology, structure, composition, and interfacial properties

The SEM image in Fig. 1a reveals TiO<sub>2</sub> particles are partially wrapped by short SWCNTs (TiO<sub>2</sub>-short SWCNT), a phenomenon that occurs uniformly over a large area on TiO<sub>2</sub> particles. EDS mapping of TiO<sub>2</sub>-short SWCNT (Fig. 1b) reveals the co-existence

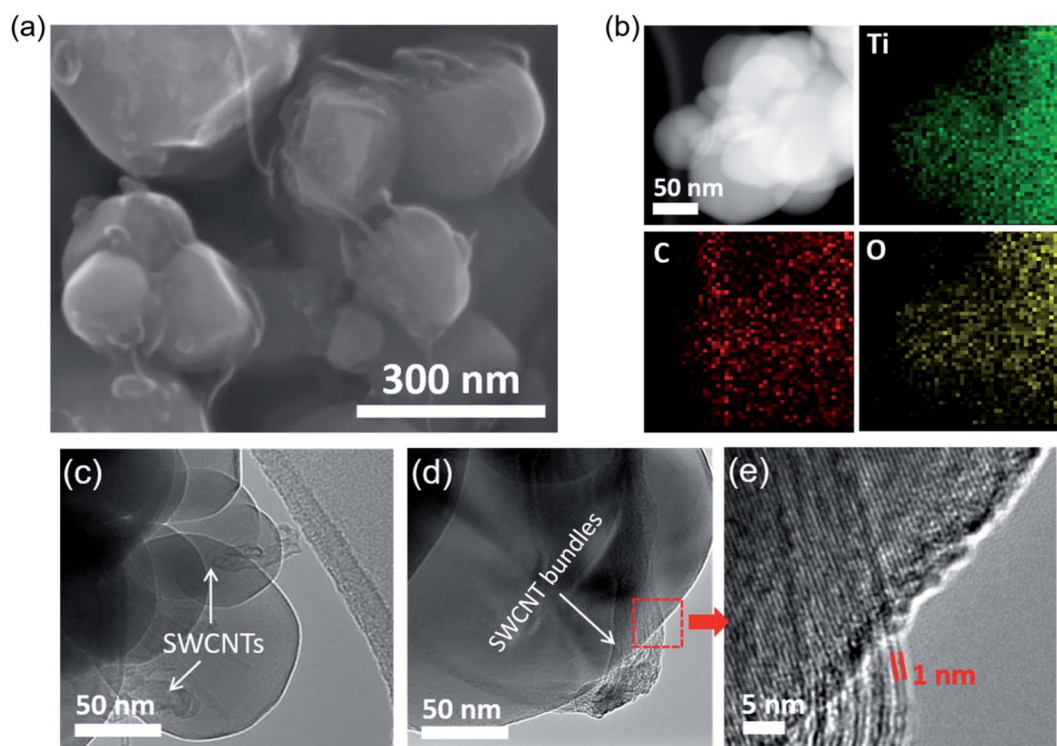


Fig. 1 (a) SEM image of TiO<sub>2</sub>-short SWCNT; (b) EDS mapping of TiO<sub>2</sub>-short SWCNT; (c) and (d) TEM images of (a) showing TiO<sub>2</sub> particles decorated with short SWCNTs and SWCNT bundles with arrows showing interactions between a TiO<sub>2</sub> particle and individual SWCNTs or bundles. (e) A zoom-in high-resolution TEM image of the region in (d) with a red square.



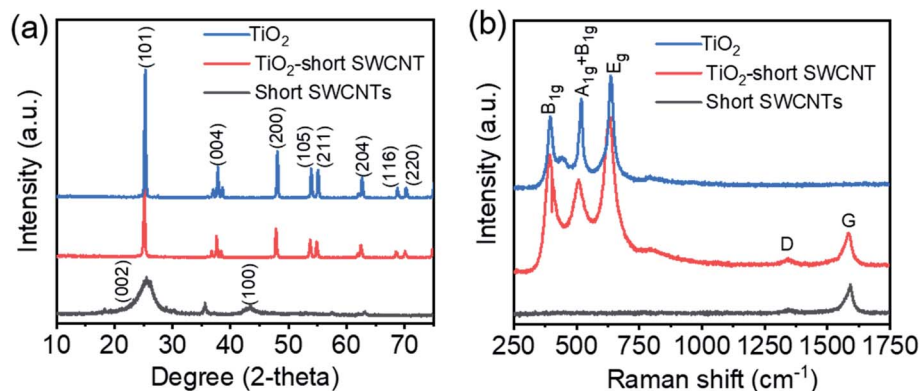


Fig. 2 (a) XRD profiles of  $\text{TiO}_2$ ,  $\text{TiO}_2$ -short SWCNT, and short SWCNTs. (b) Raman spectra of  $\text{TiO}_2$ ,  $\text{TiO}_2$ -short SWCNT, and short SWCNTs.

of carbon, titanium, and oxygen, with atomic concentrations of 15.75%, 34.23%, and 32.62%, respectively. The partial wrapping of  $\text{TiO}_2$  particles by individual SWCNTs or SWCNT bundles is further confirmed by the TEM images in Fig. 1c and d while the low-magnification SEM image in Fig. S1† demonstrates the wrapping phenomenon occurs across a large area of the sample. The TEM images (Fig. 1c and d) show short SWCNTs of different lengths either as bundles or isolated nanotubes on a  $\text{TiO}_2$  particle. From SEM and TEM data, it is apparent intimate interactions between the SWCNTs and  $\text{TiO}_2$  exist. The high-resolution TEM images in Fig. S2† show the SWCNTs form a network on  $\text{TiO}_2$  particles. The small diameters of SWCNTs ( $\sim 1.5$  nm) compared to that of  $\text{TiO}_2$  particles ( $\sim 100$  nm) implies a large fraction of the incident light can participate in excitation of  $\text{TiO}_2$ . In other words, the deposition of the short SWCNTs does not appear to lead to significant light scattering or prevent light absorption by  $\text{TiO}_2$ . However, aggregation of the short SWCNTs was observed in photocatalyst samples with higher SWCNT concentrations as shown in the  $\text{TiO}_2$ -short SWCNT sample with 3 wt% SWCNTs (Fig. S3†).

XRD patterns of short SWCNTs,  $\text{TiO}_2$ , and  $\text{TiO}_2$ -short SWCNT are shown in Fig. 2a. The peaks at  $2\theta = 55.1^\circ$ ,  $54.0^\circ$ ,  $48.1^\circ$ ,  $37.9^\circ$ , and  $25.4^\circ$  are respectively indexed to (211), (105), (200), (004), and (101) facets, typical for anatase  $\text{TiO}_2$ . The sharp and intense peaks affirm the high crystallinity of the photocatalysts, whereas the absence of peaks associated with impurities is evidence of their high quality. The peaks at  $26.8^\circ$  and  $42.8^\circ$ , usually attributed to (002) and (100) crystal planes of SWCNTs, were not detected in  $\text{TiO}_2$ -short SWCNT, due to the low SWCNT concentration (1 wt%). However, the addition of SWCNTs slightly reduced the relative intensity of  $\text{TiO}_2$  peaks, an observation consistent with other studies.<sup>46,47</sup> Raman spectra (Fig. 2b) show the characteristic peaks of anatase  $\text{TiO}_2$  at 397, 515, and  $639\text{ cm}^{-1}$ .<sup>48</sup> The characteristic anatase peaks ( $B_{1g}$ ,  $A_{1g} + B_{1g}$ , and  $E_g$ ) were observed in  $\text{TiO}_2$ -short SWCNT, accompanied by the disordered carbon-induced D-band at  $1350\text{ cm}^{-1}$ , and the G-band at  $1583\text{ cm}^{-1}$  that represents  $sp^2$  carbon from SWCNTs. The slight shift in anatase modes observed in the Raman and XRD spectra generally correlates with the external perturbation by SWCNTs and the corresponding substitution of  $\text{Ti}^{4+}$  by C atoms, resulting in the formation of Ti–O–C bonds in the  $\text{TiO}_2$

lattice.<sup>49–52</sup> However, band gaps of  $\text{TiO}_2$  and  $\text{TiO}_2$ -short SWCNT (calculated from UV-Vis spectra in Fig. S4†) are 3.22 and 3.19 eV, respectively, suggesting low-carbon doping in the composite.

An XPS survey spectrum of  $\text{TiO}_2$ -short SWCNT confirms the presence of Ti, O, and C (Fig. 3a). The high-resolution XPS spectrum of Ti 2p (Fig. 3b) shows two peaks located at 459.5 and 465.2 eV attributed to  $\text{Ti } 2p_{3/2}$  and  $\text{Ti } 2p_{1/2}$ , respectively, which are typical binding energies of the  $\text{Ti}^{4+}$  valance state.<sup>53</sup> The O 1s spectrum, shown in Fig. 3c, is fitted with three peak components. The component at 530.7 eV corresponds to Ti–O–Ti, while the peak at 531.6 eV is attributed to C=O or C–OH.<sup>53</sup> The peak at 532.8 eV is ascribed to Ti–O–C, and is an indication of the covalent interaction between  $\text{TiO}_2$  and SWCNTs.<sup>54</sup> Based on density functional theory calculations,<sup>55</sup> Ti–O–C bonds facilitate charge carrier separation due to their higher electrostatic density in comparison to the non-covalent interaction. As a consequence, the charge redistribution map predicts a higher rate of electron transport. The C 1s region, shown in Fig. 3d, is

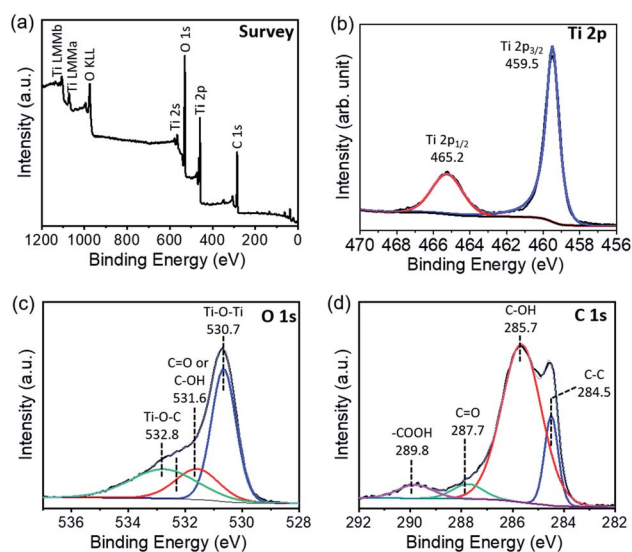


Fig. 3 XPS spectra of  $\text{TiO}_2$ -short SWCNT. (a) XPS survey spectrum; deconvolution of high-resolution Ti 2p spectrum (b), O 1s spectrum (c), and C 1s spectrum (d).



fitted with four peak components. The peak at 284.5 eV is assigned to  $sp^2$  carbon, while the peaks at 285.7, 287.7, and 289.8 eV are assigned to functional groups linked to the carbon atoms including C–O/C–O–Ti, C=O, and O–C=O, respectively.<sup>54,56</sup> The various oxygen functional groups generate anchors for direct linking with  $TiO_2$ . The absence of the Ti–C peak, typically located at 281 eV,<sup>57</sup> confirms our claim regarding the absence of significant carbon doping in the composite.

### 3.2. Photocatalytic degradation of gaseous acetaldehyde by $TiO_2$ –SWCNT hybrids

To evaluate the photocatalytic activity of  $TiO_2$  wrapped with SWCNTs, the degradation of acetaldehyde was conducted under UV light. Fig. 4a shows the effect of SWCNT amount in the hybrid structure on photocatalytic activity expressed in terms of normalized acetaldehyde concentration after 60 minutes. Coupling of short SWCNTs with  $TiO_2$  markedly improves degradation of acetaldehyde. The photocatalytic degradation activity is sensitive to the amount of SWCNTs in the composite; our findings revealed the optimum amount to be 1 wt%. A schematic illustration of the proposed mechanism for photocatalytic degradation of gaseous acetaldehyde on  $TiO_2$ –short SWCNT hybrid is depicted in Fig. 4b. Upon light illumination, photo-induced electron–hole pairs are produced by  $TiO_2$  ( $h\nu$  ( $<350$  nm)  $\rightarrow e^-_{CB+SWCNTs} + h^+$ ); the electrons are promoted to the conduction band leaving holes in the valence band.<sup>58</sup> The CB position of anatase is  $\sim 4.21$  eV using vacuum level (AVS) ( $-0.4$  eV relative to reversible hydrogen electrode (RHE)), with a bandgap of about 3.2 eV. On the other hand, the work function of a SWCNT is known to be  $\sim -4.8$  eV (AVS) (approximately 0.2 eV relative to RHE).<sup>59</sup> Since the work function of SWCNTs is lower than the conduction band of  $TiO_2$ , SWCNTs can act as electron sinks whereby a fraction of the photoelectrons flow to them.<sup>41,59</sup> The holes in the valence band react with water molecules to generate hydroxyl radicals ( $\cdot OH$ ) ( $H_2O + h^+ \rightarrow \cdot OH + H^+$ ), while the photoexcited electrons in SWCNTs and in the conduction band of  $TiO_2$  react with  $O_2$  to produce superoxide radicals ( $\cdot O_2^-$ ) ( $O_2 + e^-_{CB+SWCNTs} \Rightarrow \cdot O_2^-$ ). The active radicals initiate decomposition of adsorbed gaseous acetaldehyde *via* two

reaction pathways.  $\cdot OH$  and  $\cdot O_2^-$  could oxidize a portion of acetaldehyde to carbon dioxide and water ( $CH_3CHO \xrightarrow{\cdot OH/\cdot O_2^-} CO_2 + H_2O$ ). The remaining acetaldehyde could be oxidized to acetic acid by  $\cdot OH$  in the first step ( $CH_3CHO \xrightarrow{\cdot OH} CH_3COOH$ ) and subsequently converted to water and carbon dioxide by  $\cdot O_2^-$  in a second step ( $CH_3CHO \xrightarrow{\cdot O_2^-} CO_2 + H_2O$ ).<sup>58,60–62</sup> As shown in Fig. 4c, the relevant potential level of the acceptor species is located below the CB potential of  $TiO_2$ . On the other hand, the potential level of the donor species is above the valence band position of  $TiO_2$ , validating the generation of active radicals responsible for the degradation of gaseous acetaldehyde.<sup>63–69</sup>

It is well known the photogenerated electron–hole pair participates in redox reactions on the catalyst surface to initiate degradation of adsorbed pollutant; however, the process is limited by rapid recombination of electrons and holes. As depicted in Fig. 4b, one of the roles of SWCNTs in  $TiO_2$ –CNT composites is to inhibit electron–hole recombination.<sup>15,16</sup> An increase in the amount of SWCNTs in the hybrid composite beyond 1 wt% has a negative effect on the photocatalytic performance, which we attribute to SWCNT aggregation and generation of large SWCNT bundles. Hsu and coworkers<sup>70–75</sup> have provided further mechanistic insight into the effect of nanocarbon loading on photocatalytic performance. The overall charge separation efficiency in nanocarbon–semiconductor hybrids can be sacrificed when the amount of the electron sink (metal or nanocarbon) exceeds the optimum value. The observed trend in activity for the different  $TiO_2$ –SWCNT ratios in our study is consistent with the results from these studies and can also be rationalized by the so called later-emerging electron–hole recombination that is induced across the interface. The formation of large-diameter bundles indicates SWCNTs at high concentration tend to interact with each other *via* Van der Waals forces rather than with  $TiO_2$ . As a consequence, the quality of the interfacial contact (or degree of interaction) between  $TiO_2$  and SWCNTs is reduced. In addition, the coverage of thick SWCNT bundles on  $TiO_2$  particles has the potential of significantly decreasing light penetration to  $TiO_2$ ,

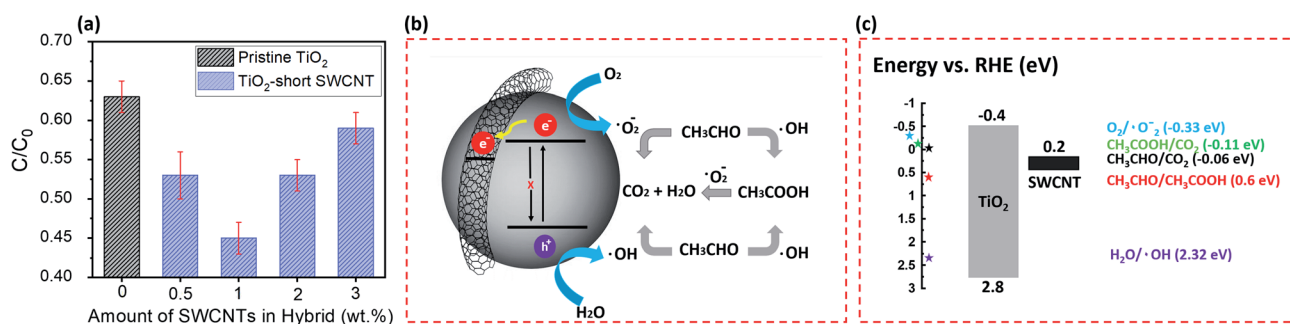


Fig. 4 (a) Photocatalytic degradation of gaseous acetaldehyde using  $TiO_2$  and  $TiO_2$ –short SWCNT of different SWCNT loadings after 60 minutes. (b) Schematic illustration of the possible mechanism of photocatalytic degradation of gaseous acetaldehyde. (c) Band edge position of a  $TiO_2$ –SWCNT hybrid relative to reversible hydrogen electrode (RHE) with approximated values of redox potentials of active radicals/compounds involved in degradation of gaseous acetaldehyde.



thus reducing photoactivity as observed in other studies that involve wrapping of graphene on TiO<sub>2</sub> or coupling graphene quantum dots with TiO<sub>2</sub>.<sup>41,76</sup> Despite the decrease in photocatalytic activity upon SWCNT aggregation, the observed performance is still higher than pristine TiO<sub>2</sub>, indicating photon permeation is not completely blocked and the beneficial role of SWCNTs in photocatalytic enhancement, *via* charge separation, may still be partially maintained.

### 3.3. Effect of SWCNT length and graphitic dimensions on interfacial contact, charge separation, and photocatalytic activity of the hybrids

To probe the influence of SWCNT length on the interfacial contact and subsequent photocatalytic performance of TiO<sub>2</sub>-SWCNT hybrids, we synthesized another composite with long SWCNTs (TiO<sub>2</sub>-long SWCNT) using the same concentration of SWCNTs, but without subjecting the sample to the ultrasonication cutting step. Representative TEM images for long SWCNTs and short SWCNTs used for coupling with TiO<sub>2</sub> are presented in Fig. S5† with corresponding box plots in Fig. 5 showing their length distributions; each box plot consists of 12 measurements of nanotubes from TEM images. The average length of short SWCNTs is  $125 \pm 90$  nm while that of long SWCNTs is  $1.2 \pm 0.67$  μm. The results clearly demonstrate the shear force generated by ultrasonication results in SWCNTs that are significantly shorter than those processed without ultrasonication. The use of ultrasonication as a nondestructive technique for cutting nanotubes is well established in processing nanomaterials. Shuba *et al.*<sup>77</sup> showed that ultrasonication yields SWCNTs with low side-wall degradation and preserves the electronic properties of the nanotubes. Note that for SWCNTs to efficiently play the intended role of “electron sink” in hybrid structures during photocatalysis, preserving their structural integrity and exceptional electronic properties is critically important.

The Raman spectra of pristine SWCNTs, short SWCNTs, and long SWCNTs in Fig. 6 provide further insight into the effect of the processing approach on the structure of SWCNTs. The ratio of G- to D-band intensities ( $I_G/I_D$ ) from the Raman spectra, widely considered a quality or graphitization index for carbon-based materials,<sup>78–80</sup> is 13.9 for pristine SWCNTs and decreases to 3.3 and 3.6 after acid treatment for long SWCNTs

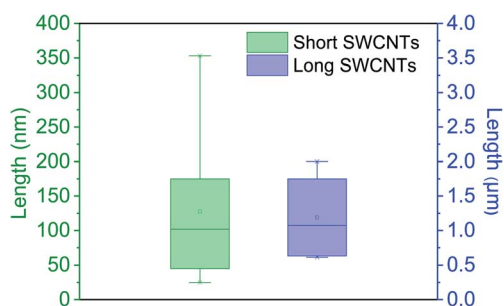


Fig. 5 Box plots showing lengths of short SWCNTs and long SWCNTs. Each box plot consists of 12 measurements of nanotubes from TEM images.

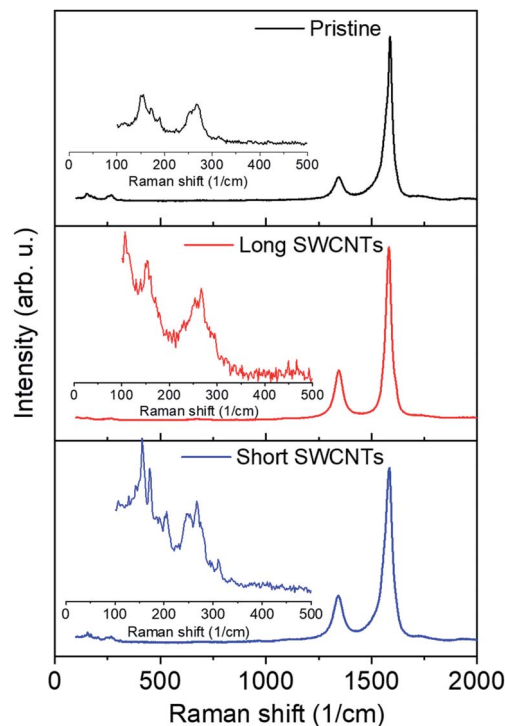


Fig. 6 Raman spectra of pristine SWCNTs, long SWCNTs and short SWCNTs with insets showing zoom-in spectra of RBMs in the lower frequency region.

and short SWCNTs, respectively, due to the functionalization of SWCNTs. The  $I_G/I_D$  ratios for short and long SWCNTs are about the same, which indicates that the ultrasonication process did not degrade the nanotubes. As observed previously in Fig. 2b, the TiO<sub>2</sub>-SWCNT composite exhibited a slight decrease in  $I_G/I_D$ , suggesting the increase in defect after the coupling of TiO<sub>2</sub> and SWCNTs,<sup>49</sup> probably due to the low substitution of Ti<sup>4+</sup> by carbon atoms. In addition, the characteristic phonon mode in SWCNTs occurring in the low frequency region (zoomed in the insets), the radial breathing mode (RBM), is clearly observed in pristine and processed SWCNTs. In fact, the same RBM peaks for pristine SWCNTs at  $\sim 150$  and  $260$  cm<sup>-1</sup> are observed for long SWCNTs and short SWCNTs. This provides further evidence that the ultrasonication process did not destroy the nanotubes.

Next, we investigate the effect of SWCNT length and nano-carbon dimension on interfacial contact, charge separation, and photocatalytic activity of the hybrids. Electron microscopic images of the resulting hybrids formed with short SWCNTs, long SWCNTs and nanographene, along with corresponding EDS mapping for TiO<sub>2</sub>-nanographene, are shown in Fig. 7. The EDS mapping of TiO<sub>2</sub>-nanographene reveal a highly uniform distribution of titanium, carbon, and oxygen as observed for TiO<sub>2</sub>-short SWCNT (Fig. 1b). In contrast to TiO<sub>2</sub>-short SWCNT (Fig. 7a), bundles of large-diameter SWCNTs are apparent in TiO<sub>2</sub>-long SWCNT composites (Fig. 7b), with severe particle aggregation as shown in Fig. S6.† These observations give credence to the assumption that ultrasonication not only reduces the length of SWCNTs, but also facilitates debundling of SWCNTs. Morphological characterization of micron-sized



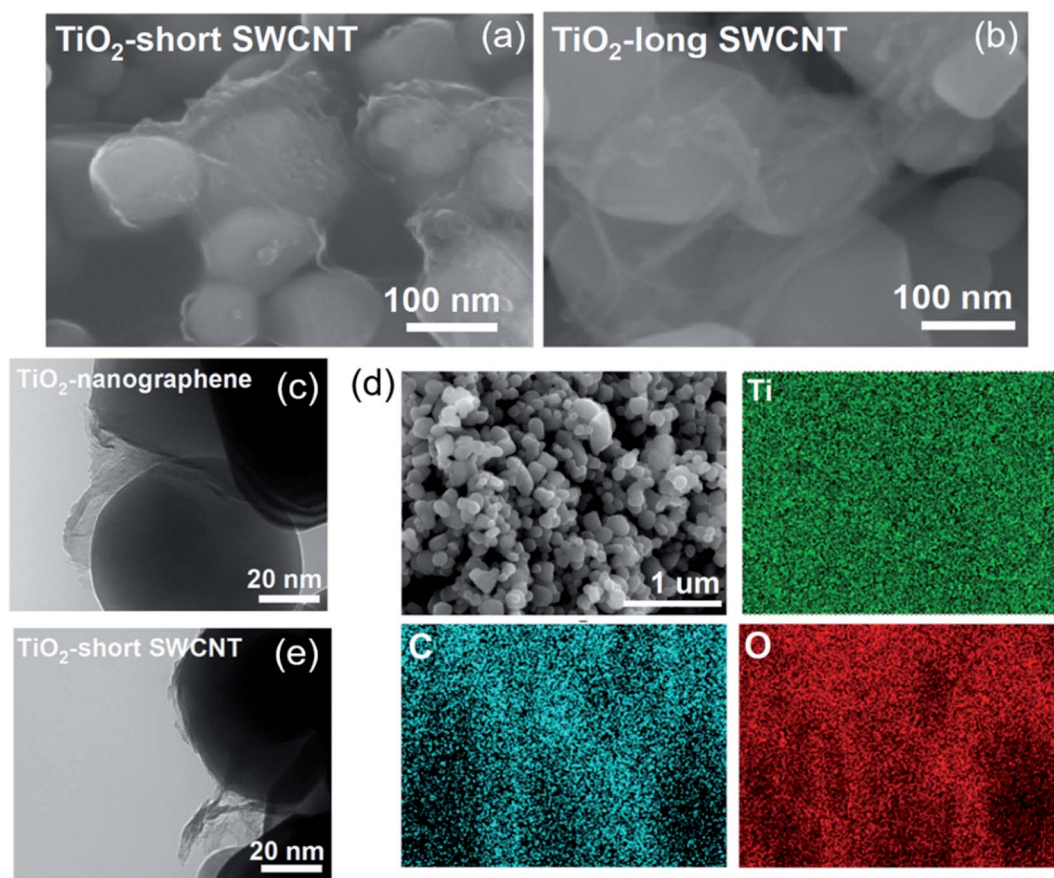


Fig. 7 SEM images of TiO<sub>2</sub>-short SWCNT (a) and TiO<sub>2</sub>-long SWCNT (b). TEM image of TiO<sub>2</sub>-nanographene (c) and corresponding EDS mapping (d). TEM image of TiO<sub>2</sub>-short SWCNT (e).

graphene, exfoliated nanographene, and non-exfoliated nanographene are summarized in Fig. S7†. The average size of the nanographene, as determined from TEM analysis and shown on the box plot (Fig. S7†), is  $\sim 125 \pm 93$  nm.

Photocatalytic degradation of acetaldehyde by TiO<sub>2</sub>, TiO<sub>2</sub>-long SWCNT, TiO<sub>2</sub>-nanographene, and TiO<sub>2</sub>-short SWCNT, is shown in Fig. 8a along with the PL spectra of the photocatalysts in Fig. 8b. As depicted in Fig. 8a, TiO<sub>2</sub>-short SWCNT shows the highest

performance; the rate constant of TiO<sub>2</sub>-short SWCNT is  $0.015 \text{ min}^{-1}$ , while others are given as follows: pristine TiO<sub>2</sub> ( $k = 0.0073 \text{ min}^{-1}$ ), TiO<sub>2</sub>-long SWCNT ( $k = 0.0107 \text{ min}^{-1}$ ), and TiO<sub>2</sub>-nanographene ( $k = 0.0125 \text{ min}^{-1}$ ). TiO<sub>2</sub>-short SWCNT showed better performance compared with TiO<sub>2</sub>-nanographene, even though the quality of interfacial contact in the two heterostructures is somewhat similar, as evidenced by EDS mapping that reveals a highly uniform distribution of nanographene on TiO<sub>2</sub> particles

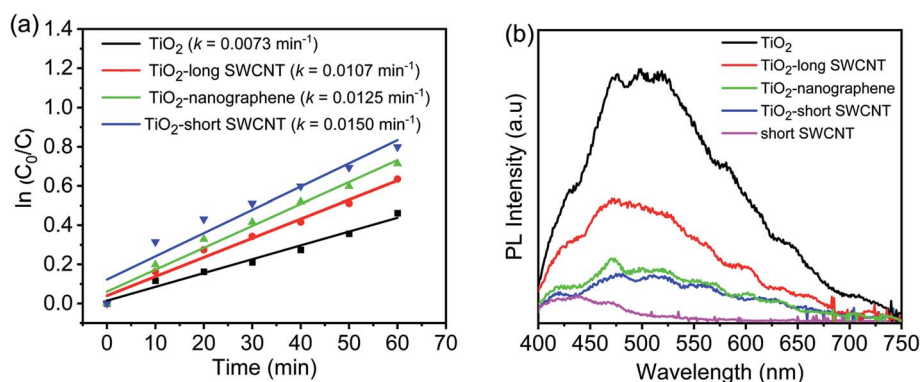


Fig. 8 (a) Photocatalytic activity of TiO<sub>2</sub>, TiO<sub>2</sub>-short SWCNT and TiO<sub>2</sub>-long SWCNT during degradation of gaseous acetaldehyde based on a pseudo first-order kinetic model. (b) Photoluminescence (PL) spectra of TiO<sub>2</sub>, TiO<sub>2</sub>-long SWCNT, TiO<sub>2</sub>-nanographene, TiO<sub>2</sub>-short SWCNT, and short SWCNT.



over a large area (Fig. 7d). The PL spectra (Fig. 8b) show lifetimes of charges on  $\text{TiO}_2$  coupled with short SWCNTs are longer than  $\text{TiO}_2$  coupled with nanographene, which explains the different photocatalytic activities observed as evidenced by their rate constants.

## 4. Discussion

Based on our results, we present a schematic illustration of the interfacial contact between nanocarbon (short SWCNTs, long SWCNTs or nanographene) and  $\text{TiO}_2$ , as well as the charge carrier movement in the hybrids in Fig. 7. We rationalize the superior performance of  $\text{TiO}_2$ -short SWCNT to be due to the inhibition of charge recombination in the composite, which can be achieved in two ways. First, the increase in the number of interfacial contacts between each individual  $\text{TiO}_2$  and short SWCNTs provides more channels for electron transport that inhibits charge recombination. The short and well-exfoliated SWCNTs can have lower bending stiffness compared to the long and non-exfoliated SWCNTs. It has been shown that bending stiffness of SWCNTs is directly proportional to SWCNT diameter;<sup>81</sup> therefore, we expect large-diameter SWCNT bundles to have larger persistence length compared to exfoliated

SWCNTs (or small-diameter SWCNT bundles). Hence, short SWCNTs efficiently wrap a  $\text{TiO}_2$  particle (Fig. 9a). Consequently, a large fraction of  $\text{TiO}_2$  nanoparticles are in direct contact with short SWCNTs. In contrast, only a small fraction of  $\text{TiO}_2$  nanoparticles are in direct contact with the long SWCNTs (Fig. 9b). Second, the improved SWCNT debundling ensures a uniform distribution of SWCNTs over a large area on the  $\text{TiO}_2$  surface, and hence, the shuttling of electrons across the interface for enhanced charge separation is not restricted to a small portion of the composite as in the case of  $\text{TiO}_2$ -long SWCNT hybrids. To test the above hypotheses, PL data presented in Fig. 8b provide valuable insight. In comparison to pristine  $\text{TiO}_2$ , fluorescence quenching was observed in the  $\text{TiO}_2$ -SWCNT hybrid structures, confirming the transfer of electrons from  $\text{TiO}_2$  to SWCNTs delayed charge recombination. It is clear from the PL results that the intensity of  $\text{TiO}_2$ -short SWCNT hybrids is lower than that of  $\text{TiO}_2$ -long SWCNT hybrids, and is substantially lower than pristine  $\text{TiO}_2$ , confirming the efficient charge separation occurring in  $\text{TiO}_2$ -short SWCNT hybrids.

To rationalize the role of short SWCNTs (or oxygen-containing functionalities), we have to consider the synthesis steps, and in particular, the zeta potentials of SWCNTs and  $\text{TiO}_2$  particles in ethanol under the pH used. Factors such as type of solvent and pH of mixture can alter the surface charge of nanostructures. In our case, acid treatment lowers the zeta potential of SWCNTs due to the formation of oxygen functionalities as shown by Liu *et al.*<sup>82</sup> These functional groups on the surface and tips of short SWCNTs imparts a strong negative charge and make them more easily dispersed. The negatively charged groups provide a strong electrostatic attraction toward positively charged species. Conversely, at low pH or high hydrogen ion activity, the surface of  $\text{TiO}_2$  acquires a positive charge due to the high zeta potential. In fact, Widegren and Bergström<sup>83</sup> showed that the addition of a relatively small amount of acid or base is capable of introducing a relatively strong charge on  $\text{TiO}_2$  particles. In our synthesis experiment,  $\text{TiO}_2$  particles and functionalized SWCNTs were dispersed in ethanol at pH = 3.5 which creates an environment with a high hydrogen activity and a strong positive charge on  $\text{TiO}_2$ . The strong positively charged  $\text{TiO}_2$  particles and negatively charged functionalized SWCNTs interact strongly *via* electrostatic attraction to form the hybrid structures with enhanced interfacial contact. In addition, opened and unblocked CNTs significantly increase the density of adsorption or anchoring sites.<sup>84</sup> Cutting of long SWCNTs increases the number of open ends, and therefore, the short SWCNTs provide more “handles” or anchoring sites for interactions with  $\text{TiO}_2$  than long SWCNTs.

The dimension of the graphitic structure is another important factor that can affect charge separation. To understand the role of the dimension of the graphitic structure in the composite, we compared the performance of  $\text{TiO}_2$  quasi-wrapped by 1D SWCNTs ( $\text{TiO}_2$ -short SWCNT) with the quasi-wrapped by 2D nanographene ( $\text{TiO}_2$ -nanographene). The synthesis of the quasi-core-shell structure is adapted from a technique proposed by Kim *et al.*<sup>36</sup> We hypothesize that random pathways in 2D graphene can significantly reduce the

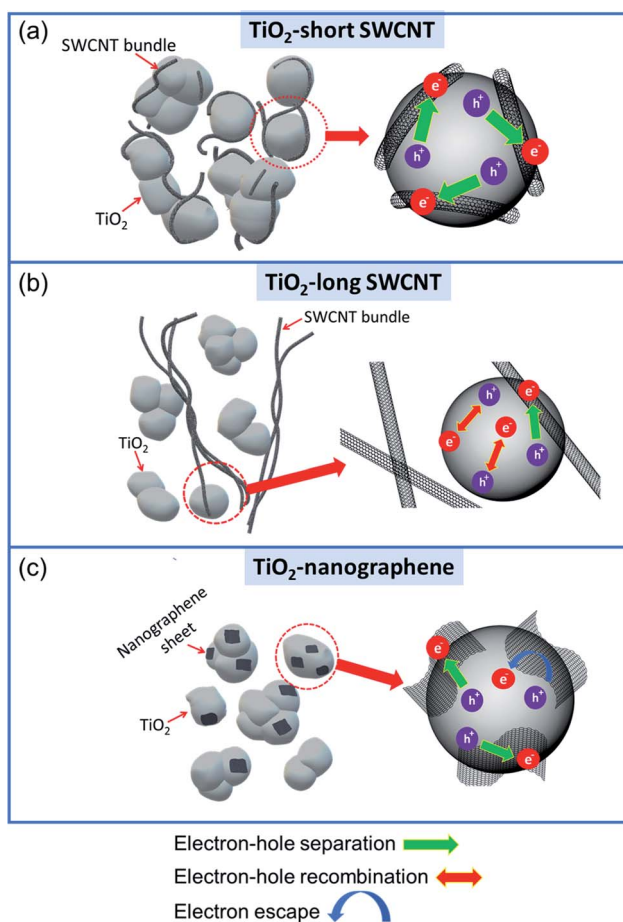


Fig. 9 Schematic illustrations of interfacial contact between nanocarbon and  $\text{TiO}_2$ , and charge carrier movement in  $\text{TiO}_2$ -short SWCNT (a),  $\text{TiO}_2$ -long SWCNT (b), and  $\text{TiO}_2$ -nanographene (c).





electron transport rate or may lead to electron escape from the graphene sheet (as schematically depicted in Fig. 9c), and thus promote charge carrier recombination. In contrast, the 1D SWCNTs offer efficient and short pathways for the transfer of vectorial electrons and, hence, enhanced charge separation. In addition, nanographene has a high stacking tendency and even after exfoliation, the number of layers cannot be easily controlled. During TEM analysis, we observed several TiO<sub>2</sub> nanoparticles with thick graphitic shells, considerably thicker than SWCNT bundles (see Fig. 7c and e). This means significant portion of incident light is hindered from reaching TiO<sub>2</sub> in a typical core-shell structure for TiO<sub>2</sub>-nanographene. On the other hand, SWCNTs, even in the case of bundles, due to their one-dimensional structure and small diameters, do not completely block light permeation to TiO<sub>2</sub>, as shown earlier for hybrid structures synthesized using high SWCNT concentrations. Nevertheless, coupling short SWCNTs or nanographene significantly improved electron-hole separation and photo-reactivity of TiO<sub>2</sub>; the photoexcited electrons in the TiO<sub>2</sub> core are efficiently transported into the nanocarbon due to the strong interfacial contact between the hybrid components.

## 5. Conclusions

TiO<sub>2</sub> nanoparticles quasi-wrapped with short SWCNTs were successfully fabricated *via* an approach that involves the interaction between TiO<sub>2</sub> and short SWCNTs in ethanol as a solvent. The presence of short SWCNTs resulted in enhanced photocatalytic activity and efficient charge separation. The improved interfacial contact, verified by electron microscopy, prolonged the lifetime of an electron-hole pair on TiO<sub>2</sub> as demonstrated by photoluminescence spectroscopy. Unlike hybrid structures with long SWCNTs, higher photocatalytic performance in gas-phase degradation of acetaldehyde was achieved with TiO<sub>2</sub>-short SWCNT hybrids, confirming use of short SWCNTs in coupling with TiO<sub>2</sub> as a better alternative. Investigations into the effect of nanocarbon dimensions on charge separation revealed TiO<sub>2</sub>-short SWCNT hybrids have slightly higher photocatalytic activity than TiO<sub>2</sub>-nanographene. We attribute the performance to electron scattering in 2D-nanographene, which may affect electron transport through the interface. The high stacking tendency of nanographene may form a thick graphitic layer on TiO<sub>2</sub> that could hinder UV light penetration. Overall, this study provides rational new guidelines for maximizing electron-hole separation in TiO<sub>2</sub>-nanocarbon hybrids for improved photocatalytic performance.

## Conflicts of interest

There are no conflicts to declare.

## Acknowledgements

This study was financially supported by the National Science Foundation (Grant No. 1653527).

## References

- 1 S.-Y. Lee and S.-J. Park, TiO<sub>2</sub> photocatalyst for water treatment applications, *J. Ind. Eng. Chem.*, 2013, **19**, 1761–1769.
- 2 A. Al Mayyahi, TiO<sub>2</sub> Polyamide Thin Film Nanocomposite Reverses Osmosis Membrane for Water Desalination, *Membranes*, 2018, **8**, 66.
- 3 Y. Sheng, Z. Wei, H. Miao, W. Yao, H. Li and Y. Zhu, Enhanced organic pollutant photodegradation *via* adsorption/photocatalysis synergy using a 3D g-C<sub>3</sub>N<sub>4</sub>/TiO<sub>2</sub> free-separation photocatalyst, *Chem. Eng. J.*, 2019, **370**, 287–294.
- 4 V. Puddu, H. Choi, D. D. Dionysiou and G. L. Puma, TiO<sub>2</sub> photocatalyst for indoor air remediation: Influence of crystallinity, crystal phase, and UV radiation intensity on trichloroethylene degradation, *Appl. Catal., B*, 2010, **94**, 211–218.
- 5 C. H. Ao and S. C. Lee, Indoor air purification by photocatalyst TiO<sub>2</sub> immobilized on an activated carbon filter installed in an air cleaner, *Chem. Eng. Sci.*, 2005, **60**, 103–109.
- 6 P. B. Amama, K. Itoh and M. Murabayashi, Gas-phase photocatalytic degradation of trichloroethylene on pretreated TiO<sub>2</sub>, *Appl. Catal., B*, 2002, **37**, 321–330.
- 7 P. B. Amama, K. Itoh and M. Murabayashi, Effect of RuO<sub>2</sub> deposition on the activity of TiO<sub>2</sub>: Photocatalytic oxidation of trichloroethylene in aqueous phase, *J. Mater. Sci.*, 2004, **39**, 4349–4351.
- 8 P. B. Amama, K. Itoh and M. Murabayashi, Photocatalytic oxidation of trichloroethylene in humidified atmosphere, *J. Mol. Catal. A: Chem.*, 2001, **176**, 165–172.
- 9 P. B. Amama, K. Itoh and M. Murabayashi, Photocatalytic degradation of trichloroethylene in dry and humid atmospheres: role of gas-phase reactions, *J. Mol. Catal. A: Chem.*, 2004, **217**, 109–115.
- 10 V. Rodríguez-González, S. Obregón, O. A. Patrón-Soberano, C. Terashima and A. Fujishima, An approach to the photocatalytic mechanism in the TiO<sub>2</sub>-nanomaterials microorganism interface for the control of infectious processes, *Appl. Catal., B*, 2020, **270**, 118853.
- 11 P. Ganguly, C. Byrne, A. Breen and S. C. Pillai, Antimicrobial activity of photocatalysts: Fundamentals, mechanisms, kinetics and recent advances, *Appl. Catal., B*, 2018, **225**, 51–75.
- 12 E. I. Cedillo-González, R. Riccò, M. Montorsi, M. Montorsi, P. Falcaro and C. Siligardi, Self-cleaning glass prepared from a commercial TiO<sub>2</sub> nano-dispersion and its photocatalytic performance under common anthropogenic and atmospheric factors, *Build Environ.*, 2014, **71**, 7–14.
- 13 Q. Yi, H. Wang, S. Cong, Y. Cao, Y. Wang, Y. Sun, Y. Lou, J. Zhao, J. Wu and G. Zou, Self-Cleaning Glass of Photocatalytic Anatase TiO<sub>2</sub>@Carbon Nanotubes Thin Film by Polymer-Assisted Approach, *Nanoscale Res. Lett.*, 2016, **11**, 457.
- 14 T. Zhu, Y. Cheng, J. Huang, J. Xiong, M. Ge, J. Mao, Z. Liu, X. Dong, Z. Chen and Y. Lai, A transparent



- superhydrophobic coating with mechanochemical robustness for anti-icing, photocatalysis and self-cleaning, *Chem. Eng. J.*, 2020, **399**, 125746.
- 15 J. Schneider, M. Matsuoka, M. Takeuchi, J. Zhang, Y. Horiuchi, M. Anpo and D. W. Bahnemann, Understanding TiO<sub>2</sub> Photocatalysis: Mechanisms and Materials, *Chem. Rev.*, 2014, **114**, 9919–9986.
- 16 K. Lee, H. Yoon, C. Ahn, J. Park and S. Jeon, Strategies to improve the photocatalytic activity of TiO<sub>2</sub>: 3D nanostructuring and heterostructuring with graphitic carbon nanomaterials, *Nanoscale*, 2019, **11**, 7025–7040.
- 17 X. Pan, Y. Zhao, S. Liu, C. L. Korzeniewski, S. Wang and Z. Fan, Comparing Graphene-TiO<sub>2</sub> Nanowire and Graphene-TiO<sub>2</sub> Nanoparticle Composite Photocatalysts, *ACS Appl. Mater. Interfaces*, 2012, **4**, 3944–3950.
- 18 W. Wang, P. Serp, P. Kalck and J. L. Faria, Visible light photodegradation of phenol on MWNT-TiO<sub>2</sub> composite catalysts prepared by a modified sol-gel method, *J. Mol. Catal. A: Chem.*, 2005, **235**, 194–199.
- 19 G. Lui, J.-Y. Liao, A. Duan, Z. Zhang, M. Fowler and A. Yu, Graphene-wrapped hierarchical TiO<sub>2</sub> nanoflower composites with enhanced photocatalytic performance, *J. Mater. Chem. A*, 2013, **1**, 12255–12262.
- 20 X. Hao, Z. Jin, J. Xu, S. Min and G. Lu, Functionalization of TiO<sub>2</sub> with graphene quantum dots for efficient photocatalytic hydrogen evolution, *Superlattices Microstruct.*, 2016, **94**, 237–244.
- 21 B. M. Everhart, M. Baker-Fales, B. McAuley, E. Banning, H. Almkhelfe, T. C. Back and P. B. Amama, Hydrothermal synthesis of carbon nanotube–titania composites for enhanced photocatalytic performance, *J. Mater. Res.*, 2020, **35**, 1451–1460.
- 22 K. Woan, G. Pyrgiotakis and W. Sigmund, Photocatalytic Carbon-Nanotube–TiO<sub>2</sub> Composites, *Adv. Mater.*, 2009, **21**, 2233–2239.
- 23 M. Shaban, A. M. Ashraf and M. R. Abukhadra, TiO<sub>2</sub> Nanoribbons/Carbon Nanotubes Composite with Enhanced Photocatalytic Activity; Fabrication, Characterization, and Application, *Sci. Rep.*, 2018, **8**, 781.
- 24 V. Štengl, D. Popelková and P. Vláčil, TiO<sub>2</sub>–Graphene Nanocomposite as High Performance Photocatalysts, *J. Phys. Chem. C*, 2011, **115**, 25209–25218.
- 25 K. Zhou, Y. Zhu, X. Yang, X. Jiang and C. Li, Preparation of graphene–TiO<sub>2</sub> composites with enhanced photocatalytic activity, *New J. Chem.*, 2011, **35**, 353–359.
- 26 A. Miribangul, X. Ma, C. Zeng, H. Zou, Y. Wu, T. Fan and Z. Su, Synthesis of TiO<sub>2</sub>/CNT Composites and its Photocatalytic Activity Toward Sudan (I) Degradation, *Photochem. Photobiol.*, 2016, **92**, 523–527.
- 27 Y. Yang, L. Xu, H. Wang, W. Wang and L. Zhang, TiO<sub>2</sub>/graphene porous composite and its photocatalytic degradation of methylene blue, *Mater. Design*, 2016, **108**, 632–639.
- 28 Z. Li, B. Gao, G. Z. Chen, R. Mokaya, S. Sotiropoulos and G. Li Puma, Carbon nanotube/titanium dioxide (CNT/TiO<sub>2</sub>) core-shell nanocomposites with tailored shell thickness, CNT content and photocatalytic/photoelectrocatalytic properties, *Appl. Catal., B*, 2011, **110**, 50–57.
- 29 J. Yu, T. Ma and S. Liu, Enhanced photocatalytic activity of mesoporous TiO<sub>2</sub> aggregates by embedding carbon nanotubes as electron-transfer channel, *Phys. Chem. Chem. Phys.*, 2011, **13**, 3491–3501.
- 30 W. Yao, Y. Li, D. Yan, M. Ma, Z. He, S. Chai, X. Su, F. Chen and Q. Fu, Fabrication and photocatalysis of TiO<sub>2</sub>-graphene sandwich nanosheets with smooth surface and controlled thickness, *Chem. Eng. J.*, 2013, **229**, 569–576.
- 31 B. Gao, C. Peng, G. Z. Chen and G. Li Puma, Photo-electrocatalysis enhancement on carbon nanotubes/titanium dioxide (CNTs/TiO<sub>2</sub>) composite prepared by a novel surfactant wrapping sol-gel method, *Appl. Catal., B*, 2008, **85**, 17–23.
- 32 X.-H. Xia, Z.-J. Jia, Y. Yu, Y. Liang, Z. Wang and L.-L. Ma, Preparation of multi-walled carbon nanotube supported TiO<sub>2</sub> and its photocatalytic activity in the reduction of CO<sub>2</sub> with H<sub>2</sub>O, *Carbon*, 2007, **45**, 717–721.
- 33 W. Zhang, G. Li, H. Liu, J. Chen, S. Ma and T. An, Micro/nano-bubble assisted synthesis of Au/TiO<sub>2</sub>@CNTs composite photocatalyst for photocatalytic degradation of gaseous styrene and its enhanced catalytic mechanism, *Environ. Sci.: Nano*, 2019, **6**, 948–958.
- 34 B. Gao, G. Z. Chen and G. Li Puma, Carbon nanotubes/titanium dioxide (CNTs/TiO<sub>2</sub>) nanocomposites prepared by conventional and novel surfactant wrapping sol-gel methods exhibiting enhanced photocatalytic activity, *Appl. Catal., B*, 2009, **89**, 503–509.
- 35 C. Wang, D. Meng, J. Sun, J. Memon, Y. Huang and J. Geng, Graphene Wrapped TiO<sub>2</sub> Based Catalysts with Enhanced Photocatalytic Activity, *Adv. Mater. Interfaces*, 2014, **1**, 1300150.
- 36 H.-i. Kim, G.-h. Moon, D. Monllor-Satoca, Y. Park and W. Choi, Solar Photoconversion Using Graphene/TiO<sub>2</sub> Composites: Nanographene Shell on TiO<sub>2</sub> Core versus TiO<sub>2</sub> Nanoparticles on Graphene Sheet, *J. Phys. Chem. C*, 2012, **116**, 1535–1543.
- 37 Y. Dai, Y. Sun, J. Yao, D. Ling, Y. Wang, H. Long, X. Wang, B. Lin, T. H. Zeng and Y. Sun, Graphene-wrapped TiO<sub>2</sub> nanofibers with effective interfacial coupling as ultrafast electron transfer bridges in novel photoanodes, *J. Mater. Chem. A*, 2014, **2**, 1060–1067.
- 38 H. R. Jafry, M. V. Liga, Q. Li and A. R. Barron, Single walled carbon nanotubes (SWNTs) as templates for the growth of TiO<sub>2</sub>: the effect of silicon in coverage and the positive and negative synergies for the photocatalytic degradation of Congo red dye, *New J. Chem.*, 2011, **35**, 400–406.
- 39 L. Ling, C. Wang, M. Ni and C. Shang, Enhanced photocatalytic activity of TiO<sub>2</sub>/single-walled carbon nanotube (SWCNT) composites under UV-A irradiation, *Sep. Purif. Technol.*, 2016, **169**, 273–278.
- 40 K. Dai, X. Zhang, K. Fan, T. Peng and B. Wei, Hydrothermal synthesis of single-walled carbon nanotube–TiO<sub>2</sub> hybrid and its photocatalytic activity, *Appl. Surf. Sci.*, 2013, **270**, 238–244.
- 41 Y. Yao, G. Li, S. Ciston, R. M. Lueptow and K. A. Gray, Photoreactive TiO<sub>2</sub>/Carbon Nanotube Composites:



- Synthesis and Reactivity, *Environ. Sci. Technol.*, 2008, **42**, 4952–4957.
- 42 R. Seshadri, H. N. Aiyer, A. Govindaraj and C. N. R. Rao, Electron transport properties of carbon nanotubes, *Solid State Commun.*, 1994, **91**, 195–199.
- 43 W. S. Hummers and R. E. Offeman, Preparation of Graphitic Oxide, *J. Am. Chem. Soc.*, 1958, **80**, 1339.
- 44 W.-C. Hu, Y.-A. Chen, P.-Y. Hsieh, C.-W. Tsao, Y.-H. Chiu, T.-F. M. Chang, C.-Y. Chen, M. Sone and Y.-J. Hsu, Reduced graphene oxides-wrapped ZnO with notable photocatalytic property, *J. Taiwan Inst. Chem. Eng.*, 2020, **112**, 337–344.
- 45 K.-A. Tsai and Y.-J. Hsu, Graphene quantum dots mediated charge transfer of CdSe nanocrystals for enhancing photoelectrochemical hydrogen production, *Appl. Catal., B*, 2015, **164**, 271–278.
- 46 Y. Huang, D. Chen, X. Hu, Y. Qian and D. Li, Preparation of TiO<sub>2</sub>/Carbon Nanotubes/Reduced Graphene Oxide Composites with Enhanced Photocatalytic Activity for the Degradation of Rhodamine B, *Nanomaterials*, 2018, **8**, 431.
- 47 Y. Li, Z. Wang and X.-J. Lv, N-doped TiO<sub>2</sub> nanotubes/N-doped graphene nanosheets composites as high performance anode materials in lithium-ion battery, *J. Mater. Chem. A*, 2014, **2**, 15473–15479.
- 48 F. Wang and K. Zhang, Physicochemical and photocatalytic activities of self-assembling TiO<sub>2</sub> nanoparticles on nanocarbons surface, *Curr. Appl. Phys.*, 2012, **12**, 346–352.
- 49 B. Chai, T. Peng, X. Zhang, J. Mao, K. Li and X. Zhang, Synthesis of C60-decorated SWCNTs (C60-d-CNTs) and its TiO<sub>2</sub>-based nanocomposite with enhanced photocatalytic activity for hydrogen production, *Dalton Trans.*, 2013, **42**, 3402–3409.
- 50 T. Appadurai, C. M. Subramaniam, R. Kuppusamy, S. Karazhanov and B. Subramanian, Electrochemical Performance of Nitrogen-Doped TiO<sub>2</sub> Nanotubes as Electrode Material for Supercapacitor and Li-Ion Battery, *Molecules*, 2019, **24**, 2952.
- 51 W. Li, R. Liang, N. Y. Zhou and Z. Pan, Carbon Black-Doped Anatase TiO<sub>2</sub> Nanorods for Solar Light-Induced Photocatalytic Degradation of Methylene Blue, *ACS Omega*, 2020, **5**, 10042–10051.
- 52 R. Taziwa, E. L. Meyer and K. G. Chinyama, Raman temperature dependence analysis of carbon-doped titanium dioxide nanoparticles synthesized by ultrasonic spray pyrolysis technique, *J. Mater. Sci.*, 2012, **47**, 1531–1540.
- 53 G. An, W. Ma, Z. Sun, Z. Liu, B. Han, S. Miao, Z. Miao and K. Ding, Preparation of titania/carbon nanotube composites using supercritical ethanol and their photocatalytic activity for phenol degradation under visible light irradiation, *Carbon*, 2007, **45**, 1795–1801.
- 54 W. Vallejo, A. Rueda, C. Díaz-Urbe, C. Grande and P. Quintana, Photocatalytic activity of graphene oxide–TiO<sub>2</sub> thin films sensitized by natural dyes extracted from *Bactris guineensis*, *R. Soc. Open Sci.*, 2019, **6**, 181824.
- 55 S. Ayissi, P. A. Charpentier, K. Palotás, N. Farhangi, F. Schwarz and W. A. Hofer, Preferential Adsorption of TiO<sub>2</sub> Nanostructures on Functionalized Single-Walled Carbon Nanotubes: A DFT Study, *J. Phys. Chem. C*, 2015, **119**, 15085–15093.
- 56 Z. Hu, Y. Huang, S. Sun, W. Guan, Y. Yao, P. Tang and C. Li, Visible light driven photodynamic anticancer activity of graphene oxide/TiO<sub>2</sub> hybrid, *Carbon*, 2012, **50**, 994–1004.
- 57 H. Wu, J. Fan, E. Liu, X. Hu, Y. Ma, X. Fan, Y. Li and C. Tang, Facile hydrothermal synthesis of TiO<sub>2</sub> nanospindles-reduced graphene oxide composite with a enhanced photocatalytic activity, *J. Alloys Compd.*, 2015, **623**, 298–303.
- 58 Q. Zeng, X. Xie, X. Wang, Y. Wang, G. Lu, D. Y. H. Pui and J. Sun, Enhanced photocatalytic performance of Ag@TiO<sub>2</sub> for the gaseous acetaldehyde photodegradation under fluorescent lamp, *Chem. Eng. J.*, 2018, **341**, 83–92.
- 59 Y. Yao, G. Li, S. Ciston, R. M. Lueptow and K. A. Gray, Photoreactive TiO<sub>2</sub>/Carbon Nanotube Composites: Synthesis and Reactivity, *Environ. Sci. Technol.*, 2008, **42**, 4952–4957.
- 60 H. Hu, W.-j. Xiao, J. Yuan, J.-w. Shi, M.-x. Chen and W.-f. Shang Guan, Preparations of TiO<sub>2</sub> film coated on foam nickel substrate by sol-gel processes and its photocatalytic activity for degradation of acetaldehyde, *J. Environ. Sci.*, 2007, **19**, 80–85.
- 61 X. Ye, D. Chen, J. Gossage and K. Li, Photocatalytic oxidation of aldehydes: Byproduct identification and reaction pathway, *J. Photochem. Photobiol., A*, 2006, **183**, 35–40.
- 62 A. H. Mamaghani, F. Haghighat and C.-S. Lee, Photocatalytic oxidation technology for indoor environment air purification: The state-of-the-art, *Appl. Catal., B*, 2017, **203**, 247–269.
- 63 H. Huang, B. Pradhan, J. Hofkens, M. B. J. Roeflaers and J. A. Steele, Solar-Driven Metal Halide Perovskite Photocatalysis: Design, Stability, and Performance, *ACS Energy Lett.*, 2020, **5**, 1107–1123.
- 64 X. Zhao, L. Du, B. You and Y. Sun, Integrated design for electrocatalytic carbon dioxide reduction, *Catal. Sci. Technol.*, 2020, **10**, 2711–2720.
- 65 R. D. Feinman, Oxidation-reduction calculations in the biochemistry course, *Biochem. Mol. Biol. Educ.*, 2004, **32**, 161–166.
- 66 W. He, H.-K. Kim, W. G. Wamer, D. Melka, J. H. Callahan and J.-J. Yin, Photogenerated Charge Carriers and Reactive Oxygen Species in ZnO/Au Hybrid Nanostructures with Enhanced Photocatalytic and Antibacterial Activity, *J. Am. Chem. Soc.*, 2014, **136**, 750–757.
- 67 A. L. Linsebigler, G. Lu and J. T. Yates, Photocatalysis on TiO<sub>2</sub> Surfaces: Principles, Mechanisms, and Selected Results, *Chem. Rev.*, 1995, **95**, 735–758.
- 68 M.-J. Fang, C.-W. Tsao and Y.-J. Hsu, Semiconductor nanoheterostructures for photoconversion applications, *J. Phys. D: Appl. Phys.*, 2020, **53**, 143001.
- 69 Y.-H. Chiu, T.-F. M. Chang, C.-Y. Chen, M. Sone and Y.-J. Hsu, Mechanistic Insights into Photodegradation of Organic Dyes Using Heterostructure Photocatalysts, *Catalysts*, 2019, **9**, 430.
- 70 Y.-C. Chen, K.-i. Katsumata, Y.-H. Chiu, K. Okada, N. Matsushita and Y.-J. Hsu, ZnO–graphene composites as practical photocatalysts for gaseous acetaldehyde



- degradation and electrolytic water oxidation, *Appl. Catal., A*, 2015, **490**, 1–9.
- 71 Y.-C. Chen, Y.-C. Pu and Y.-J. Hsu, Interfacial Charge Carrier Dynamics of the Three-Component  $\text{In}_2\text{O}_3$ - $\text{TiO}_2$ -Pt Heterojunction System, *J. Phys. Chem. C*, 2012, **116**, 2967–2975.
- 72 Y.-H. Hsu, A. T. Nguyen, Y.-H. Chiu, J.-M. Li and Y.-J. Hsu, Au-decorated GaOOH nanorods enhanced the performance of direct methanol fuel cells under light illumination, *Appl. Catal., B*, 2016, **185**, 133–140.
- 73 W.-H. Lin, Y.-H. Chiu, P.-W. Shao and Y.-J. Hsu, Metal-Particle-Decorated ZnO Nanocrystals: Photocatalysis and Charge Dynamics, *ACS Appl. Mater. Interfaces*, 2016, **8**, 32754–32763.
- 74 Y.-F. Lin and Y.-J. Hsu, Interfacial charge carrier dynamics of type-II semiconductor nanoheterostructures, *Appl. Catal., B*, 2013, **130–131**, 93–98.
- 75 Y.-C. Pu, H.-Y. Chou, W.-S. Kuo, K.-H. Wei and Y.-J. Hsu, Interfacial charge carrier dynamics of cuprous oxide-reduced graphene oxide ( $\text{Cu}_2\text{O}$ -rGO) nanoheterostructures and their related visible-light-driven photocatalysis, *Appl. Catal., B*, 2017, **204**, 21–32.
- 76 D. Pan, J. Jiao, Z. Li, Y. Guo, C. Feng, Y. Liu, L. Wang and M. Wu, Efficient Separation of Electron–Hole Pairs in Graphene Quantum Dots by  $\text{TiO}_2$  Heterojunctions for Dye Degradation, *ACS Sustainable Chem. Eng.*, 2015, **3**, 2405–2413.
- 77 M. V. Shuba, A. G. Paddubskaya, P. P. Kuzhir, S. A. Maksimenko, V. K. Ksenevich, G. Niaura, D. Seliuta, I. Kasalynas and G. Valusis, Soft cutting of single-wall carbon nanotubes by low temperature ultrasonication in a mixture of sulfuric and nitric acids, *Nanotechnology*, 2012, **23**, 495714.
- 78 L. Bokobza, J.-L. Bruneel and M. Couzi, Raman Spectra of Carbon-Based Materials (from Graphite to Carbon Black) and of Some Silicone Composites, *Carbon*, 2015, **1**, 77–94.
- 79 S. Santangelo, Controlled surface functionalization of carbon nanotubes by nitric acid vapors generated from sub-azeotropic solution, *Surf. Interface Anal.*, 2016, **48**, 17–25.
- 80 P. B. Amama, C. Lan, B. A. Cola, X. Xu, R. G. Reifenberger and T. S. Fisher, Electrical and Thermal Interface Conductance of Carbon Nanotubes Grown under Direct Current Bias Voltage, *J. Phys. Chem. C*, 2008, **112**, 19727–19733.
- 81 N. Fakhri, D. A. Tsyboulski, L. Cognet, R. B. Weisman and M. Pasquali, Diameter-dependent bending dynamics of single-walled carbon nanotubes in liquids, *Proc. Natl. Acad. Sci.*, 2009, **106**, 14219.
- 82 Y. Liu, L. Gao, J. Sun and Y. Wang, Functionalization of carbon nanotubes for nanoparticle attachment, *J. Ceram. Process. Res.*, 2010, **11**, 120–122.
- 83 J. Widegren and L. Bergström, Electrostatic Stabilization of Ultrafine Titania in Ethanol, *J. Am. Ceram. Soc.*, 2004, **85**, 523–528.
- 84 X. Ren, C. Chen, M. Nagatsu and X. Wang, Carbon nanotubes as adsorbents in environmental pollution management: A review, *Chem. Eng. J.*, 2011, **170**, 395–410.

